CLIMATOLOGY

A multicentennial mode of North Atlantic climate variability throughout the Last Glacial Maximum

Matthias Prange[1]*, Lukas Jonkers[1], Ute Merkel[1], Michael Schulz[1], Pepijn Bakker[2]

Paleoclimate proxy records from the North Atlantic region reveal substantially greater multicentennial temperature variability during the Last Glacial Maximum (LGM) compared to the current interglacial. As there was no obvious change in external forcing, causes for the increased variability remain unknown. Exploiting LGM simulations with a comprehensive coupled climate model along with high-resolution proxy records, we introduce an oscillatory mode of multicentennial variability, which is associated with moderate variations in the Atlantic meridional overturning circulation and depends on the large-scale salinity distribution. This self-sustained mode is amplified by sea-ice feedbacks and induces maximum surface temperature variability in the subpolar North Atlantic region. Characterized by a distinct climatic imprint and different dynamics, the multicentennial oscillation has to be distinguished from Dansgaard-Oeschger variability and emerges only under full LGM climate forcing. The potential of multicentennial modes of variability to emerge or disappear in response to changing climate forcing may have implications for future climate change.

INTRODUCTION

Climate variability at multicentennial scales is poorly understood but has important implications for attributing past changes and predicting future climate trends (*1*, *2*). The understanding of climate variability is complicated by its dependence on the climatic mean state (*3*). Paleoclimate proxy records have shown substantial changes in climate variability before and after Termination I, the last major transition in global mean climate (*4*). During the Last Glacial Maximum (LGM) [approximately 23 to 19 ka (kiloyears before present)] before Termination I, temperature variability at multicentennial time scales was globally about four times larger than afterward during the Holocene (*4*). By far, the greatest change in variability between glacial and interglacial climate was found in the northern North Atlantic region, where Greenland ice cores reveal particularly strong multicentennial temperature variability in the ~300- to 800-year band throughout the LGM (Fig. 1, A to C). A sea surface temperature (SST) record with sufficiently high temporal resolution and chronological constraints from the adjacent Irminger Sea (sediment core SO82-5) also reveals pronounced multicentennial variations during the LGM that have been correlated with Greenland ice core records (*5*). In particular, the SST record shows three distinct peaks after Heinrich Stadial 2 (HS 2) between ~23 and ~21.5 ka (Fig. 1D), where the first one appears to be related to Dansgaard-Oeschger (DO) event 2, an uncharacteristically weak and short DO event compared to its marine isotope stage (MIS) 3 counterparts (*6*, *7*). Smaller SST variations are found before and after these peaks (Fig. 1D). This high multicentennial variability found in LGM SST records from the subpolar North Atlantic was previously postulated to be linked to continuous DO cyclicity over MIS 2 (*8*), whereas other studies argue for a minor influence of DO cyclicity on LGM climate variability (*4*, *9*).

However, the spatiotemporal coverage of SST time series is still insufficient to resolve patterns of multicentennial climate variability during the LGM. There are only few records with sufficient temporal resolution, and their analysis is further complicated by dating uncertainties. Moreover, the simulation of low-frequency climate variability to investigate underlying physical mechanisms is still a challenge for general circulation models (*1*, *10*). Causes and mechanisms of the high multicentennial LGM temperature variability in the Greenland and subpolar North Atlantic regions are therefore still unknown (*4*). As there is no obvious external forcing on this time scale, internal mechanisms are the most likely cause of this variability. Here, we present a mechanism of spontaneous multicentennial oscillations in the North Atlantic realm found in simulations with the Community Earth System Model CESM1.2 under LGM boundary conditions (see Materials and Methods). We demonstrate that this mode of variability is specific to the LGM and disappears if the boundary conditions deviate from full glacial conditions. We further show that this type of climate variability has to be distinguished from DO variability as it clearly differs in terms of spatial pattern, magnitude, time scale, and dynamics.

Besides the (oscillating) reference experiment LGM_{ref}, three sensitivity experiments (LGM_{210}, LGM_{199}, and LGM_{176}) were performed to explore the role of atmospheric greenhouse gas (GHG) concentrations for the oscillatory behavior (Table 1). Experiment LGM_{IC} examines the role of different initial conditions using the same boundary conditions as experiment LGM_{ref}. Experiment $LGM_{IC,GHG}$ uses still another initialization, while GHG concentrations are slightly different but still characteristic for the LGM. Last, experiment LGM_{ICE6G} was set up to explore the role of ice sheets using the ICE-6G_C reconstruction (*11*) instead of GLAC-1D (*12*–*14*). Experiment LGM_{ICE6G} was supplemented by GHG sensitivity experiments $LGM_{ICE6G,210}$, $LGM_{ICE6G,199}$, and $LGM_{ICE6G,176}$ that use the same set of GHG concentrations as the corresponding sensitivity experiments with GLAC-1D ice sheet. Both GLAC-1D and ICE-6G_C ice sheets used in this study refer to the 21-ka time slice. No prescribed meltwater fluxes were added such that simulated oscillations are "unhosed." Table 1 summarizes the experiments.

[1]MARUM–Center for Marine Environmental Sciences, University of Bremen, Bremen, Germany. [2]Department of Earth Sciences, Vrije Universiteit Amsterdam, Amsterdam, Netherlands.
*Corresponding author. Email: mprange@marum.de

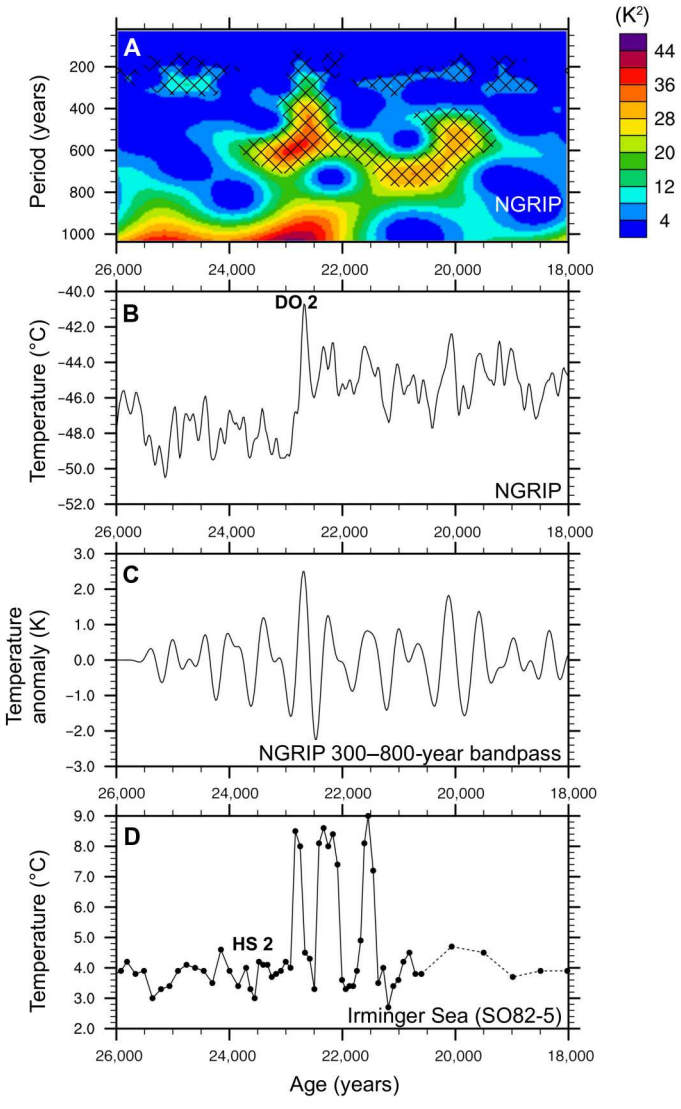

Fig. 1. Evidence of multicentennial variability at high northern latitudes during the LGM. Reconstructed temperatures for the North Greenland Ice Core Project (NGRIP) site are based on $\delta^{15}N$ isotope measurements on the ss09sea06bm time scale (*7*). (**A**) Wavelet (Morlet) power spectrum of the NGRIP temperature time series shown in (**B**) for the interval of 26 to 18 ka. Hatching indicates the 0.01 significance level using a red noise background (*72*). (**C**) Temperature time series from (B) bandpass-filtered for the 300 to 800 years range using a zero-phase sixth-order Butterworth filter. The bandpass filter highlights the multicentennial component in the NGRIP record and reveals the amplitude of the multicentennial temperature oscillations. (**D**) Summer SST reconstruction from Irminger Sea sediment core SO82-5 (*5*) on a new age scale (*69*). For ages younger than about 20.5 ka, the temporal resolution of the record is not sufficient to capture multicentennial variability (dashed curve). HS 2 and DO 2 are marked. Locations of NGRIP and SO82-5 are shown in Fig. 3B.

RESULTS

The mean Atlantic meridional overturning circulation (AMOC) in experiment LGM_{ref}, averaged over the entire 1540 years of the experiment, has a weaker and shallower upper overturning cell (Fig. 2A) compared to a preindustrial control run of the model (fig. S1A) (*15*). The simulated glacial Atlantic is characterized by strong salinity stratification in the deep ocean (Fig. 2B). Shoaling of glacial North Atlantic deep water and a stronger stratification are consistent with reconstructions (*16*, *17*). Moreover, there is proxy-based evidence for more saline Antarctic bottom water (*18*, *19*) and relatively fresh and shallow Antarctic intermediate water (AAIW) (*20*) during the LGM, which corroborates the simulated water mass characteristics. We note that a high-saline deep ocean has been suggested previously as a prerequisite for the glacial termination (*21*). A multicentennial oscillation of the AMOC around this mean state is revealed by the time series of the AMOC index, defined here as the maximum of the overturning stream function at 30°N. Within the 1540 years of integration, four cycles are found, i.e., a period of ~400 years (Fig. 3A). The peak-to-peak amplitude of the oscillation is about 4 Sv (1 Sv = 10^6 m^3 s^{-1}). Despite this moderate amplitude of AMOC variations, there is a clear impact on North Atlantic sea-ice extent and Greenland temperature (Fig. 3, A to C). During a strong AMOC interval, annual mean surface air temperature in central Greenland is about 4°C warmer than during a weak AMOC interval. The magnitude of the simulated temperature variations is thus comparable to the reconstructed North Greenland Ice Core Project (NGRIP) temperature variations at the multicentury scale (Fig. 1C). In addition, the long-term LGM mean temperature at the NGRIP site (Fig. 1B) is well reproduced by the model. Even larger surface air temperature contrasts between strong and weak AMOC intervals are found south of Iceland and over the Irminger Sea associated with a retreat (expansion) of the North Atlantic sea-ice margin during the strong (weak) AMOC phase (Fig. 3, B and C), which leads to a reduction (increase) in surface albedo and an increase (decrease) in ocean-atmosphere surface heat fluxes (see below). While the wintertime northern North Atlantic is largely ice-covered during intervals of weak AMOC (Fig. 3C), vast areas in the Nordic Seas are ice-free in summer during strong AMOC intervals (Fig. 3B). The sea-ice feedbacks are crucial for inducing particularly large surface air temperature variations in the northern North Atlantic region, over Greenland, and over parts of Europe. The rest of the globe is hardly affected. In particular, the AMOC oscillations are too small in amplitude and too short in duration to induce a global-scale bipolar seesaw pattern. The same is true for precipitation, where substantial changes are only simulated over the North Atlantic and parts of Greenland and western Europe, while changes in other regions, such as the tropics, are insignificant (Fig. 3C). In the global annual mean, the multicentennial oscillation causes a surface air temperature variation in the range of 0.8 K (fig. S2). Note that no such multicentennial oscillations are found in the preindustrial control run (fig. S1B).

The leading empirical orthogonal functions (EOFs) of various ocean variables provide further insight into the spatiotemporal dynamics of the multicentennial oscillation. Figure 4 shows the first EOFs of North Atlantic winter mixed layer depth, sea-ice fraction, surface heat flux, SST, and ocean temperature at 1000 m in depth. The principal components covary with the AMOC time series. A short lag of the AMOC index with respect to changes in North Atlantic surface variables is attributable to the duration of dynamic adjustment to North Atlantic convection accomplished by internal ocean waves (*22*, *23*). Hence, deepening of the mixed layer in the North Atlantic is directly related to enhanced convection and a strengthening of the AMOC (Fig. 4A), whereby the AMOC index lags ~20 years behind the leading principal component of mixed

Table 1. Summary of experiments. See Materials and Methods for further details including description of initialization methods.

Experiment	CO_2 (ppm)	CH_4 (ppb)	N_2O (ppb)	Ice sheet	Initialization method	Integration length (years)
LGM_{ref}	187.2	375.0	206.5	GLAC-1D	1	1540
LGM_{210}	210.4	556.1	256.1	GLAC-1D	1	620
LGM_{199}	198.8	465.6	231.3	GLAC-1D	1	1620
LGM_{176}	175.6	284.4	181.7	GLAC-1D	1	1180
LGM_{IC}	187.2	375.0	206.5	GLAC-1D	2	1840
$LGM_{IC,GHG}$	187.4	381.7	205.1	GLAC-1D	3	2861
LGM_{ICE6G}	187.2	375.0	206.5	ICE-6G_C	1	640
$LGM_{ICE6G,210}$	210.4	556.1	256.1	ICE-6G_C	1	1240
$LGM_{ICE6G,199}$	198.8	465.6	231.3	ICE-6G_C	1	820
$LGM_{ICE6G,176}$	175.6	284.4	181.7	ICE-6G_C	1	720

layer depth (fig. S3). Enhanced convection, in turn, is associated with increased ocean surface heat loss under reduced sea-ice conditions (Fig. 4, B and C). When the AMOC is strong, winter sea ice disappears south of Iceland and in the Irminger Sea (cf. Fig. 3B), allowing for deep convection, while the region becomes winter sea ice–covered when the AMOC is weak (cf. Fig. 3C). While AMOC strengthening goes along with North Atlantic sea-ice retreat and higher SSTs (Fig. 4D), subsurface temperatures decrease over large regions, including the Irminger Sea (Fig. 4E).

Temporal changes of the large-scale salinity distribution play a key role in the dynamics of the multicentennial oscillation. Figure 5A shows the first EOF of equatorial and North Atlantic salinity at 400 m, which is about the depth of the shallow and fresh glacial AAIW (cf. Fig. 2B). The leading EOF (the time series of which lags behind the AMOC variations as seen in the right panel of Fig. 5A) indicates a large-scale freshening of the North Atlantic equatorial and subtropical regions in response to a strengthening of the AMOC, most strongly pronounced between 5°N and 10°N off the South American coast. As the AMOC is directly related to meridional velocities, the leading principal component of upper-ocean (400 m in depth) meridional velocity in the tropical Atlantic covaries with the AMOC index (Fig. 5B, right). The strongest variations are found off the South American coast (Fig. 5B). It has been shown previously that the western boundary currents in this region are highly sensitive to changes in the AMOC (*24*). A northward current along the South American coast, which transports glacial AAIW across the equator into the North Atlantic, therefore corresponds to a glacial version of the modern Intermediate Western Boundary Current (*25*). Variations in this current system, as revealed by the EOF analysis (Fig. 5B), result in transport variations of the relatively fresh glacial AAIW into the northern hemisphere and hence control the North Atlantic salinity budget. These freshwater transports explain freshening of the North Atlantic tropical and subtropical regions in response to AMOC strengthening (Fig. 5A). Maximum salinity variations between 5°N and 10°N off the South American coast are attributable to the combination of strong meridional velocity variations (Fig. 5B) with a steep meridional salinity gradient (Fig. 2B). The freshwater accumulating in the subtropical North Atlantic (Fig. 5A) eventually reaches the northern North Atlantic, where it enters the convective regions and, through its effect on density, leads to a weakening of the AMOC.

The sequence of processes causing the North Atlantic climate oscillation is depicted in Fig. 6. An increasing AMOC goes along with a decreasing net salinity flux across 5°N toward the subtropical North Atlantic due to an increasing northward transport of low-saline water in the upper intermediate western Atlantic (Fig. 6A). As a consequence, the tropical-subtropical North Atlantic gradually freshens (Fig. 6B). This freshening, in turn, results in a decreasing salinity flux across 35°N into the northern North Atlantic (Fig. 6A). This anomalously low-salinity flux eventually leads to a freshening of the convective regions, hence weakening the AMOC. The weaker AMOC reduces the northward flow of fresh glacial AAIW, thus leading to an increasing net salinity flux across 5°N toward the subtropical region, such that the tropical-subtropical North Atlantic salinity increases. An increased salinity flux into the northern North Atlantic amplifies the AMOC again, thereby closing the oscillation cycle. These processes clearly suggest a salt-oscillator mechanism as the main cause for the multicentennial oscillations, which is also supported by the meridional propagation of Atlantic salinity anomalies over an oscillation cycle (Fig. 7 and fig. S4).

While freshening of the upper northern North Atlantic leads to enhanced density stratification, increased sea-ice cover, and reduced convective mixing (Fig. 4), advective and diffusive heat fluxes cause the subsurface ocean to gradually warm up, thereby increasing the vertical temperature gradient (Fig. 6B). While this tends to counteract the density stratification (*26*), the vertical density gradient still increases because of salinity changes (Fig. 6B). Another positive feedback mechanism we identified is related to the strength of the North Atlantic subpolar gyre, which favors deep-water formation by transporting salt toward the convective regions. Similar to previous studies (*27*, *28*), the subpolar gyre covaries with the AMOC (fig. S5). However, in its simplest form, the salt-oscillator mechanism also works without these feedbacks as shown by a simple box model that consists of two coupled ordinary differential equations (ODEs), which describe salinity changes in a subpolar and a subtropical ocean box (see Materials and Methods and fig. S6). In this two-box model, the inflow of low-saline AAIW into the subtropical box is a crucial element. Oscillatory solutions with

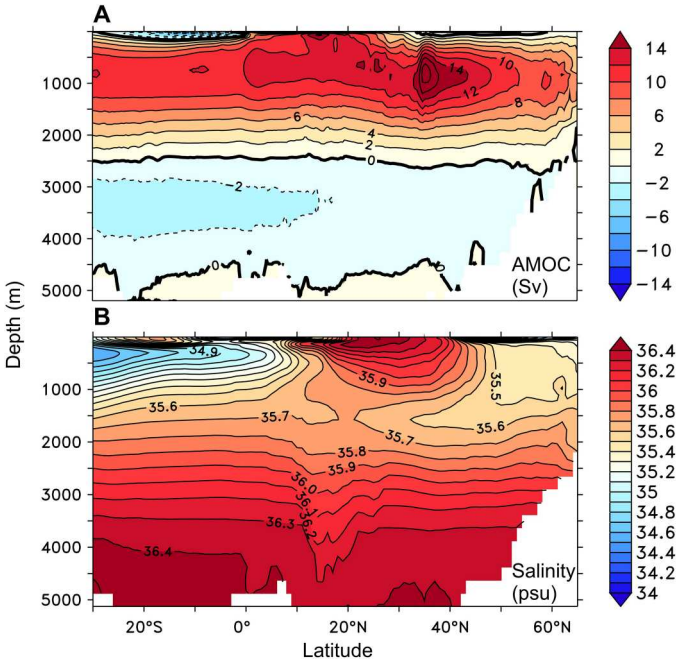

Fig. 2. Atlantic Ocean mean state in the LGM_{ref} simulation. (**A**) Atlantic meridional overturning stream function. Negative (positive) contour lines are dashed (solid) and indicate counterclockwise (clockwise) flow direction. (**B**) Zonally averaged Atlantic salinity. Shown are averages over 1540 years. Note the presence of a shallow, low-saline AAIW tongue with a core around 400 m in depth.

multicentennial period (~400 years) can only occur if the AMOC transports sufficiently fresh AAIW into the subtropical box (fig. S7A). If the salinity of the AAIW is too high, then the oscillations disappear (fig. S7B).

Sensitivity experiments were conducted to explore the influence of changes in boundary conditions on the multicentennial oscillation. In a first set of experiments, atmospheric GHG concentrations were varied, ranging from MIS 3 conditions (experiment LGM_{210}) via intermediate (LGM_{199}) to extremely low (LGM_{176}) conditions (see Materials and Methods). Moderate shifts in GHG concentrations away from LGM values in experiments LGM_{199} and LGM_{176} cause the multicentennial North Atlantic climate and AMOC variability to be suppressed (Fig. 8), suggesting that the oscillations only exist in a very narrow range around full LGM boundary conditions. GHG concentrations exceeding those of the LGM reference concentrations (as listed in Table 1) amplify the hydrologic cycle in the warmer atmosphere (*29*), such that net evaporation over the subtropical North Atlantic increases. As a result, surface salinity rises in the North Atlantic (fig. S8A). In combination with a poleward retreat of the sea-ice margin and enhanced surface heat loss in the northern North Atlantic, this favors deep convection and pushes the AMOC into a strong stable state (Fig. 8), although more low-salinity glacial AAIW is transported toward the subtropical North Atlantic as revealed by the Atlantic salinity distribution (fig. S8A). The opposite processes occur in the cold climate scenario of experiment LGM_{176} (fig. S8B), such that the AMOC adopts a weak steady state (Fig. 8). In sum, we find a disappearance of the multicentennial oscillatory mode for non-LGM GHG concentrations along with a general trend of increasing AMOC strength with larger GHG forcing.

Minor changes in LGM boundary conditions with respect to LGM_{ref}, however, do not remove the multicentennial oscillation dynamics as demonstrated by experiment $LGM_{IC,GHG}$. Along with experiment LGM_{IC}, this experiment further shows that LGM multicentennial oscillations are robust to changing initial conditions (fig. S9).

Last, experiment LGM_{ICE6G} reveals that the multicentennial mode is suppressed when the ICE-6G_C reconstruction is applied (Fig. 8). The major difference of ICE-6G_C compared to GLAC-1D is a higher ice elevation over North America, which is up to ~1 km at some locations (*14*). The higher Laurentide ice sheet has an impact on the atmospheric circulation including a southward displacement of the North Atlantic mid-latitude jet in line with previous model studies (*30*, *31*). Moreover, the North Atlantic wind-driven ocean circulation changes, implying southward shifting subtropical and subpolar gyres (fig. S10), which hampers the transport of salty waters from the subtropics toward convective regions in the northern North Atlantic. The resulting fresher conditions in these regions prevent phases of strong convection required for the multicentennial oscillation to occur. While we suggest a role of gyre transports in suppressing the multicentennial mode, this does not rule out a potential role of other processes, such as changes in precipitation and evaporation patterns (*32*), effects of surface cooling (*33*), or changes in deep-water formation regions in response to ice sheet alterations (*34*). Regardless of the mechanism, the sensitivity to ice sheet height may explain why previous LGM simulations with the same climate model (CESM1.2) but other ice sheet boundary conditions than GLAC-1D did not exhibit multicentennial climate oscillations (*35*, *36*).

Additional sensitivity experiments with the same ICE-6G_C ice sheet configuration but different GHG forcing ($LGM_{ICE6G,210}$, $LGM_{ICE6G,199}$, and $LGM_{ICE6G,176}$) did not show the multicentennial oscillation either (fig. S11). While this does not rule out the possibility of multicentennial oscillations under ICE-6G_C for other parameter ranges, we note that further studies are required for a more complete understanding of the role of ice sheet height in suppressing low-frequency oscillations. Moreover, as in the GHG sensitivity experiments with GLAC-1D, we find again that the AMOC strengthens with increasing GHG forcing (fig. S11).

The multicentennial oscillation of experiment LGM_{ref} has its largest imprint on the surface climate in the northern North Atlantic region (Fig. 3, B and C). Figure 9A shows the variance of low pass–filtered simulated North Atlantic SST. Besides some hot spots of high variability in the subpolar and mid-latitude North Atlantic, there is a general trend of decreasing variance from the northern to the tropical North Atlantic. Only a few paleo-SST records from North Atlantic sediment cores exist that have high enough temporal resolution and sufficient age control to be analyzed in terms of multicentennial variability during the LGM (see Materials and Methods). Analyzing these records for variance at the multicentury scale, we find a qualitative agreement between the latitudinal patterns of modeled and reconstructed variances in that the SST proxy records also reveal high variability in subpolar and mid-latitudes and almost no variance in low latitudes (Fig. 9B). This confirms the model result that multicentennial variability during the LGM was predominantly a North Atlantic phenomenon. By contrast, this pronounced multicentennial variability is absent in both the CESM1.2 preindustrial control run (*15*) and SST proxy records from the late Holocene (fig. S12). Moreover, it is also

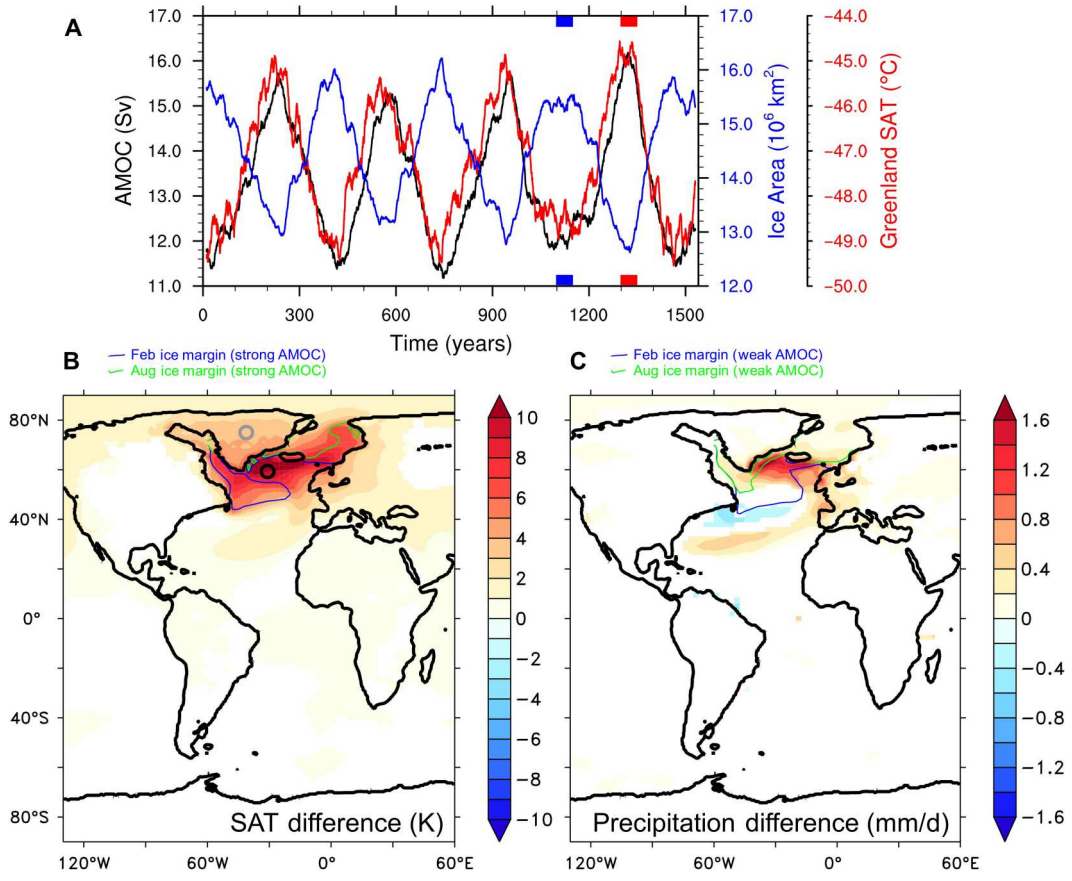

Fig. 3. Climate signature of North Atlantic multicentennial mode in the LGM_{ref} simulation. (**A**) Time series of AMOC strength (defined as the maximum of Atlantic overturning stream function at 30°N; black), Northern Hemisphere total sea-ice area (blue), and surface (2 m) air temperature (SAT) at NGRIP site (red). All time series are smoothed with a 21-year running mean. The time axis refers to the model integration years of the LGM_{ref} experiment after spin up. (**B**) Mean (50-year averages) surface air temperature difference between strong AMOC interval [marked by red bars in (A)] and weak AMOC interval [marked by blue bars in (A)]. Blue (green) line shows the February (August) mean sea-ice margin (defined here as the 50% ice concentration contour line) for the strong AMOC interval. (**C**) Same as (B) but for precipitation. Here, blue and green lines refer to February and August sea-ice margins for the weak AMOC interval. In (B) and (C), differences are only shown if statistically significant at the 0.05 level. In (B), circles over Greenland and in the Irminger Sea mark the locations of the NGRIP ice core (gray) and the SO82-5 marine sediment core (black). Continental outlines according to GLAC-1D.

found that the modeled SST variances are generally lower than the proxy-based variances during both the LGM and the late Holocene. Part of this discrepancy may be related to local processes that cannot be resolved by the global model, such as amplification of SST variations due to changes in coastal upwelling or frontal shifts. An impact of other modes of large-scale climate variability or external forcing mechanisms, not included or underestimated in the model simulation, cannot be ruled out either (*1*). On the other hand, nonclimatic noise and possible proxy-specific biases might lead to an overestimation of the SST variance derived from marine sediment archives (*37*), which would be consistent with the good agreement between the magnitudes of simulated and reconstructed multicentennial temperature variations over Greenland from the NGRIP ice core (see above).

DISCUSSION

Multicentennial glacial climate variability has been little explored so far. We presented an internal mode of multicentennial North Atlantic variability simulated in a comprehensive coupled climate model under full LGM boundary conditions. The multicentennial mode is associated with self-sustained AMOC oscillations that are relatively small compared to the millennial-scale DO oscillations of MIS 3. While model-based estimates for DO-type AMOC variations of MIS 3 are about 10 Sv (*38*) or even higher (*39*–*41*), the range of multicentennial AMOC variations is only ~4 Sv in experiment LGM_{ref}.

Only few proxy records exist that have a temporal resolution high enough to capture climate variability at this time scale. The Irminger SST record of core SO82-5 suggests several oscillation cycles following HS 2, before a reduction in the record's resolution around 20.5 ka prevents any detection of multicentennial oscillations. The SST record of sediment core MD95-2002 from the northern Bay of Biscay (*42*) shows further multicentennial oscillations after 20.5 ka (fig. S13). Sea surface salinity reconstructions from core SO82-5 show high-saline conditions during warm multicentennial phases and fresher conditions during cold phases (*5*), in agreement with our simulated oscillations. Unlike the millennial-scale DO cycles of MIS 3 (DO 3 to 17), which had a global impact on climate (*43*), the LGM multicentennial mode is primarily

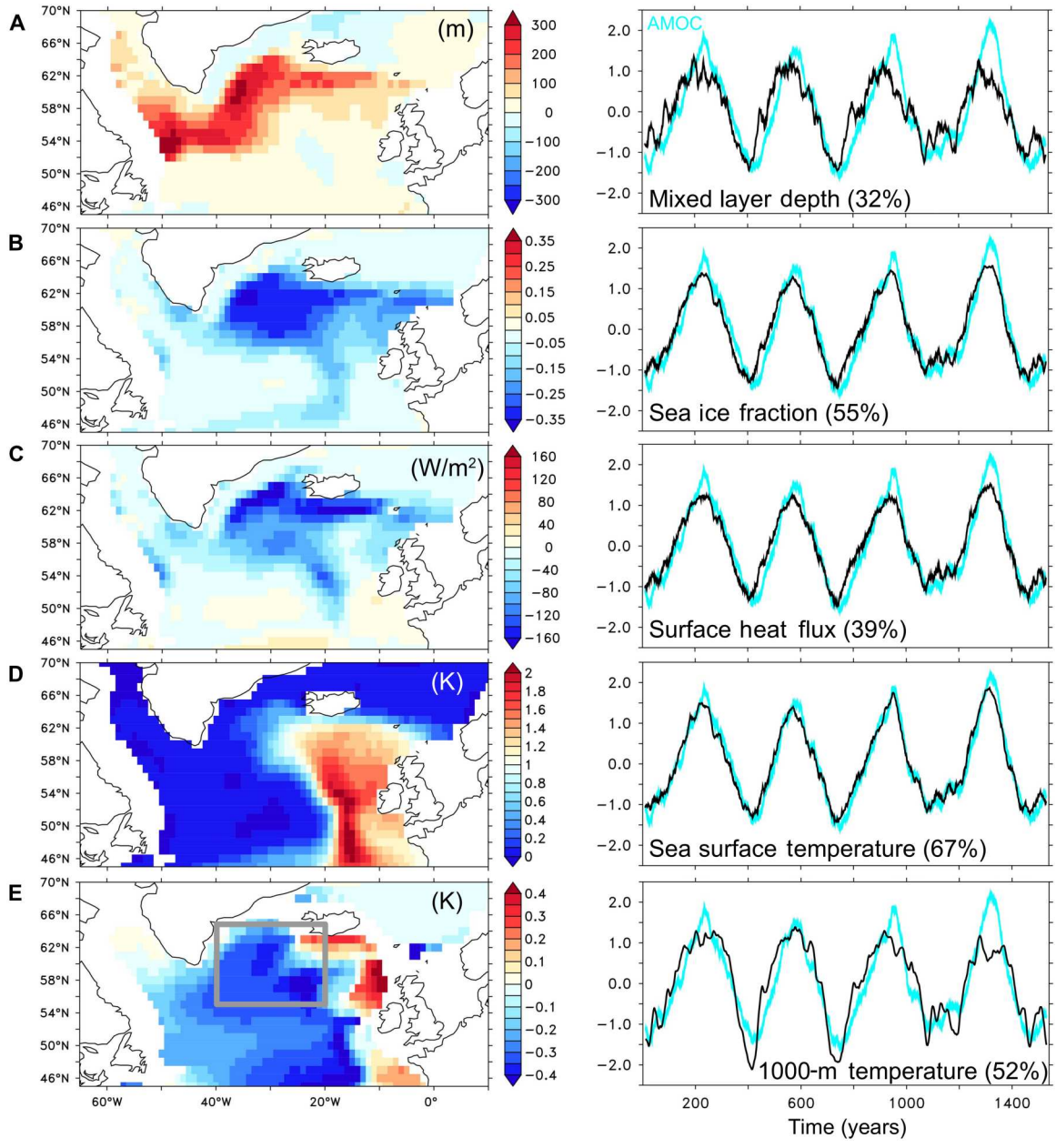

Fig. 4. EOF analysis of various winter mean (January to March) ocean variables from the LGM_{ref} simulation and relation to AMOC variations. Leading EOFs for the North Atlantic region are shown for (**A**) mixed layer depth, (**B**) sea-ice concentration, (**C**) surface heat flux, (**D**) SST (note that the color code only resolves positive values in the map), and (**E**) potential temperature at 1000 m in depth. EOF maps (left) were obtained by regressing the fields onto the corresponding standardized (dimensionless) principal component time series (right). The standardized principal component time series (black) are plotted together with the standardized AMOC time series (as defined in Fig. 3; cyan). Explained variances of each leading EOF are specified below the time series. Gray box in (E) marks approximately the region of maximum variations in sea-ice cover and surface heat flux, which is used for calculating averages in Fig. 6B. In this region, a strong (weak) AMOC is associated with an anomalously deep (shallow) mixed layer, low (high) sea-ice concentration, high (low) surface heat flux from the ocean to the atmosphere, high (low) SST, and prevailing low (high) 1000-m subsurface temperatures.

a North Atlantic phenomenon, contributing to the generally higher climate variability in northern high latitudes during the LGM than today (fig. S14) (*4*).

Given the more regional character and shorter time scale, the multicentennial mode must be clearly distinguished from the millennial-scale DO mode. Moreover, warming and cooling phases of the multicentennial oscillation are of nearly equal duration, whereas DO cycles are characterized by an abrupt transition from cold to warm states and a slow transition from warm to cold states (*44*). The different spatiotemporal patterns and amplitudes of AMOC variation point to different modes of operation, although the millennial-scale DO mode may also rely on a meridional salt oscillation as suggested previously (*41*, *44*–*46*).

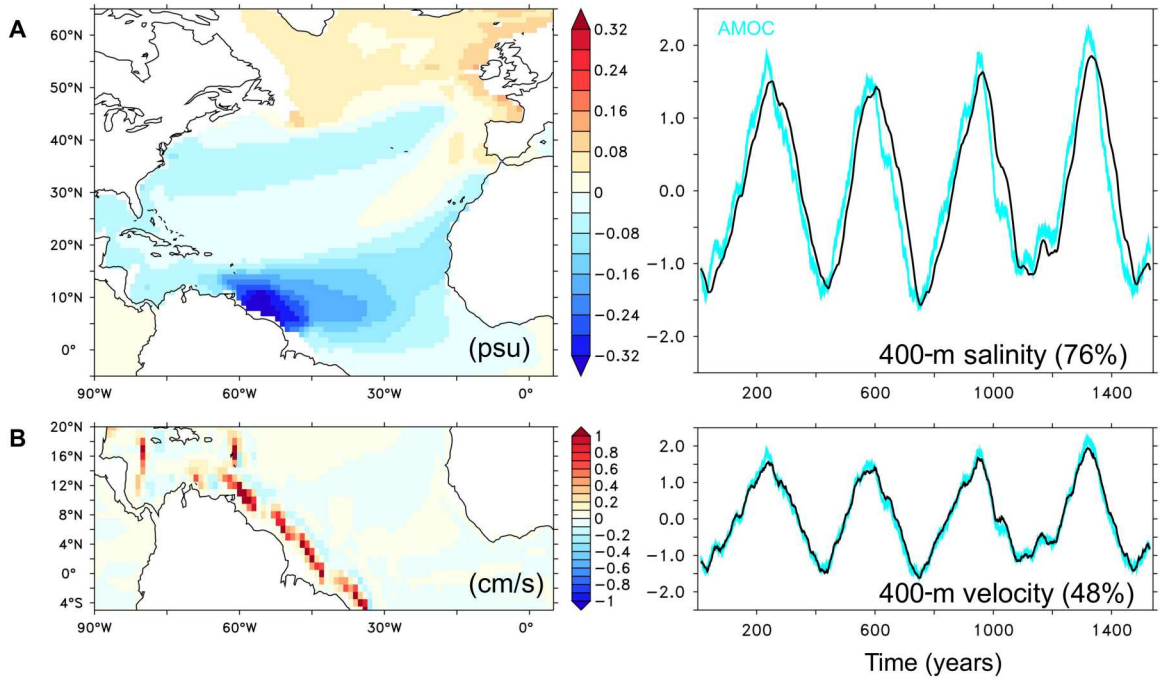

Fig. 5. EOF analysis for salinity and meridional velocity at 400 m in depth and relation to AMOC variations. Leading EOFs for different regions are shown for (**A**) annual mean salinity and (**B**) annual mean meridional velocity (positive means northward). The depth of 400 m corresponds to the location of glacial AAIW (cf. Fig. 2B). Methods applied as in Fig. 4. The standardized (dimensionless) principal component time series (black) are plotted together with the standardized AMOC time series (as defined in Fig. 3; cyan). The EOFs indicate a freshening of the tropical and subtropical North Atlantic in response to an increased northward transport of low-saline glacial AAIW along the South American coast associated with an increased AMOC and vice versa (note that the EOF time series of salinity lags behind the AMOC variations).

A key characteristic of a DO-type cycle is the formation of a strong halocline in the North Atlantic covered by a winter sea-ice lid extending southward to the Bay of Biscay during the cold stadial phase (*28*, *44*, *47*–*49*). This suppresses surface heat loss from the subpolar ocean and prevents convection and deep-water formation. Without convective mixing, the subsurface ocean warms by up to 5 K (*28*, *44*, *45*). Erosion of the strong halocline takes several centuries, where the exact mechanism appears to differ between models (*50*). Subsurface warming may also destabilize the vertical stratification (*26*, *28*, *45*, *51*). Eventually, an abrupt recovery of convection sets in by a thermohaline instability, which, in some models, is associated with the formation of an extensive polynya south of Greenland (*28*, *47*, *51*). This sets the stage for the fast transition from the stadial to the interstadial DO phase associated with a massive release of heat accumulated for centuries from the subsurface reservoir in a "thermohaline flush" and the development of an exceedingly strong AMOC, which weakens only slowly during the interstadial "relaxation" phase (*41*, *44*, *48*). Again, details of the relaxation dynamics differ among models (*50*).

While variations in surface salinity, sea-ice cover, convection, and subsurface temperatures also play a role for the multicentennial oscillation, the magnitude of these variations is substantially smaller than in the simulated DO-type variability (*28*, *41*, *44*). Our LGM_{ref} simulation reveals several key regions of winter convective mixing in the northern North Atlantic (fig. S15). Convective mixing covaries with the multicentennial oscillation in all the regions except for the northern Labrador Sea where winter convection is active but decoupled from the multicentennial variability. In contrast to a DO-type cycle, we suspect that steady Labrador Sea convection always

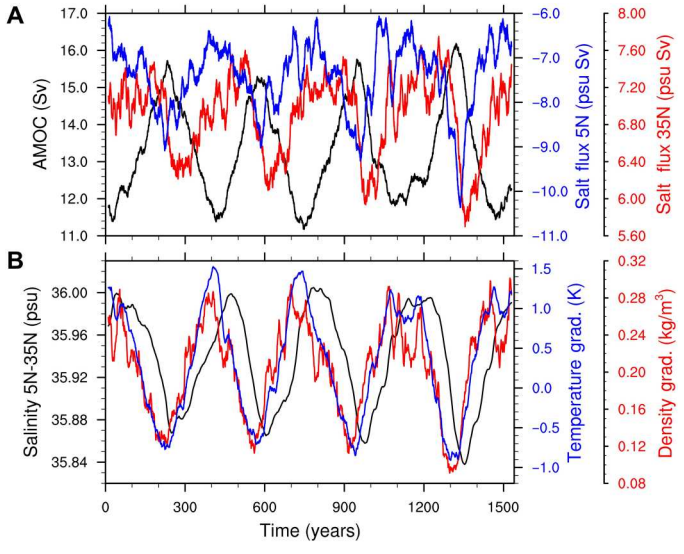

Fig. 6. Time series of ocean variables playing a key role in the multicentennial oscillation mechanism. (**A**) Time series of AMOC strength (as defined in Fig. 3; black), total integrated northward advective salinity flux in the Atlantic across 5°N (blue) and across 35°N (red). (**B**) Time series of subtropical Atlantic salinity (averaged zonally over the entire Atlantic, latitudinally from 5°N to 35°N and vertically over the top 1000 m; black), vertical temperature gradient in the North Atlantic (blue), and vertical potential density gradient in the North Atlantic (red). Vertical gradients are defined as the difference between 1000 m and the surface of the corresponding variable and averaged over the box depicted in Fig. 4E (40°W to 20°W, 55°N to 65°N; region of maximum variations in sea-ice cover and surface heat flux). All time series are smoothed with a 21-year running mean. See main text for a detailed description of the oscillation mechanism.

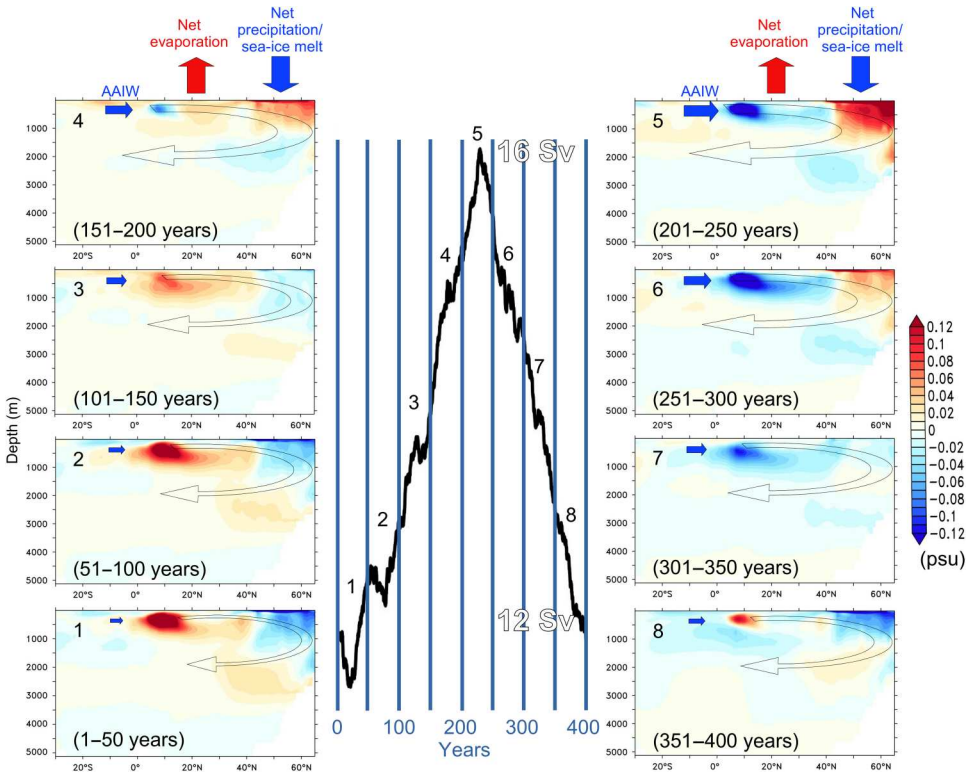

Fig. 7. Salt-oscillator mechanism of multicentennial mode illustrated by changes in the Atlantic salt distribution over one oscillation cycle. The middle panel depicts the time series of AMOC strength over the first 400 years in experiment LGM_{ref}, comprising the first oscillation cycle (cf. Fig. 6A). Panels 1 to 8 show the evolution of zonally averaged Atlantic salinity anomalies (with respect to the 400-year mean) as consecutive 50-year averages. Size of the curved black arrow symbolizes the strength of the AMOC during each 50-year chunk. Size of the horizontal blue arrow indicates the magnitude of shallow, low-saline glacial AAIW transport. A weak AMOC in panel 1 is associated with relatively fresh subpolar conditions in the upper ocean. High tropical/subtropical salinities result from a reduced glacial AAIW transport into the North Atlantic. The oceanic salinity flux from the subtropics into the subpolar convective regions is high during this phase, leading to a gradual increase in subpolar upper-ocean salinity and AMOC strength (panels 2 to 4). With the stronger AMOC, more low-saline AAIW is transported northward, resulting in a freshening of the North Atlantic tropics/subtropics (panel 5). The salinity transport from the subtropics to the subpolar regions is therefore low during this phase, which, in combination with net precipitation and sea-ice melt, leads to a gradual decrease in subpolar upper-ocean salinity and AMOC strength (panels 5 to 8).

maintains a substantial overturning circulation and hampers the formation of an overly strong DO-type stadial halocline. As a result, moderate salinity flux anomalies from the subtropics are sufficient to bring moderately reduced deep-water formation and AMOC back into high gear (Fig. 6A). We thus hypothesize that persistent local winter convection is instrumental for the multicentennial mode and constitutes a key difference to DO-type AMOC oscillations that have larger magnitudes and longer periods. In this conceptual framework, subpolar North Atlantic conditions would modify the dynamics of the low-frequency mode, while meridional salt oscillations would be the driver.

The LGM oscillatory mode we introduce in the present study also appears to be distinct from multicentennial modes described in previous climate model studies under modern boundary conditions. Those modes were attributed to Southern Ocean/Weddell Sea "flip-flop oscillations" driven by subsurface ocean heat content variations (*52*–*56*) or "loop oscillations," which are linked to the advection of salinity anomalies by the deep overturning (*57*–*60*). Recent modeling studies suggested mechanisms of multicentennial AMOC variability driven by salinity anomalies that build up in the upper layers of the Arctic Ocean and are eventually released into the North Atlantic deep-water formation regions (*61*–*63*). By contrast, we found no role of the Arctic Ocean in driving the LGM multicentennial mode as variations in Arctic Ocean salinity and salinity fluxes out of the Arctic do not vary at this time scale (fig. S16). Instead, the multicentennial mode we suggest here relies on the transport of particularly fresh and shallow AAIW that is specific to the glacial ocean. Moreover, we suggest that the existence of this mode depends sensitively on the North Atlantic freshwater balance, such that moderate deviations of the boundary conditions (GHG concentrations and ice sheet geometry) from LGM conditions lead to its suppression.

In this study, we presented results from model experiments with fixed boundary conditions. As a logical next step, transient simulations that take into account varying boundary conditions over the LGM interval should be conducted. These boundary conditions would include moderate variations in GHG concentrations, orbital parameters, ice sheets, meltwater, solar, and volcanic forcing. We speculate that the multicentennial oscillations would become less regular because of the varying forcing, possibly matching the noisier variability found in the NGRIP record (cf. Fig. 1) more closely.

Modes of climate variability can change, emerge, or disappear in response to changing climate forcing and boundary conditions.

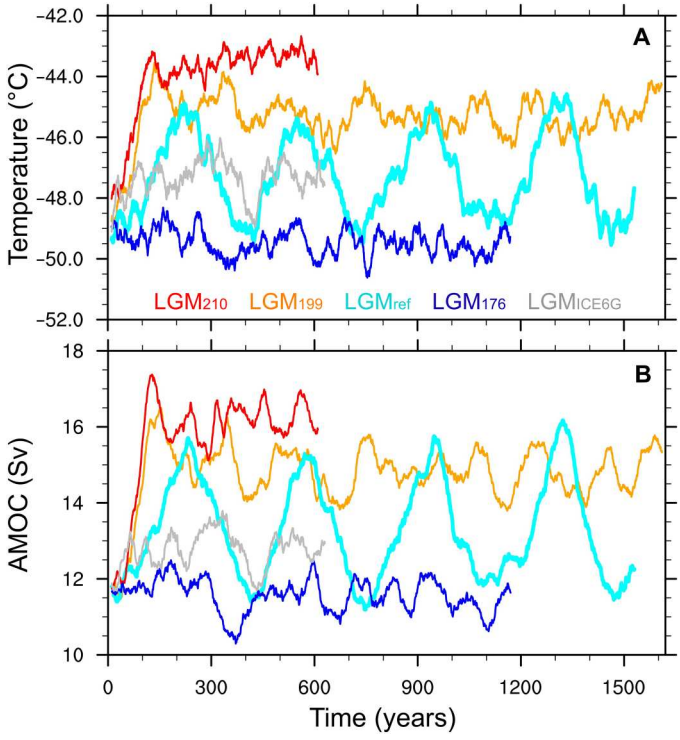

Fig. 8. Effect of different boundary conditions (GHG concentrations and ice sheet geometry) on climate and AMOC state. (**A**) Time series of Greenland surface air temperature at NGRIP site and (**B**) AMOC strength as defined in Fig. 3. Different colors refer to different experiments applying different GHG concentrations (LGM_{210}, red; LGM_{199}, orange; LGM_{ref}, cyan; LGM_{176}, dark blue) and ice sheet configuration (LGM_{ICE6G}, gray). All time series are smoothed with a 21-year running mean. All simulations start with the same initial conditions; hence, there is a spin-up phase at the beginning of each sensitivity experiment.

This study suggests the emergence of an internal multicentennial mode under conditions much colder than present day. Similarly, new modes of variability may arise or existing modes may be suppressed under future warmer conditions. Here, we suggest a salt-oscillator mechanism that necessitates appropriate freshwater budgets. It cannot be ruled out that a sweet spot for multicentennial oscillations can also be attained under other climate conditions—both colder and warmer than present day—that create the required salinity gradients. A much deeper understanding of climate variability on time scales ranging from years to millennia must be acquired, as the emergence of new or previously undetected modes of variability could have implications for future climate change.

MATERIALS AND METHODS

Climate model experiments

The fully coupled CESM1.2 (*64*) includes the Community Atmosphere Model (CAM5), the Community Land Model (CLM4.0), the Parallel Ocean Program (POP2), and the Community Ice Code (CICE4). In all our CESM experiments, we use a horizontal resolution of 1.9° latitude by 2.5° longitude with 30 levels in the atmosphere. The ocean and sea-ice components share the same horizontal grid with a nominal 1° resolution and the North Pole displaced over Greenland. The ocean grid has 60 levels in the vertical. The time step of the atmosphere model is 30 min, while the ocean model has a time step of 1 hour. Model analysis is based on monthly mean output. Analysis of ocean and sea-ice model output was preceded by a remapping of the fields from the model grid to a regular 1° latitude-longitude grid. The land model uses the same horizontal resolution as the atmosphere and includes a representation of the carbon-nitrogen cycle. This allows the prognostic and interactive simulation of leaf and stem area indices and vegetation height, although the vegetation biogeography is fixed as in a previous study (*65*).

LGM boundary conditions refer to the 21-ka time slice, remain fixed throughout each model experiment, and include GHG concentrations, insolation changes due to orbital parameters, ice sheet extent, land surface elevations, and land-sea mask, resulting in the closure of several key ocean passages, such as the Bering Strait. POP2's overflow parameterization is applied in Denmark Strait and the Iceland-Scotland region as in Brady *et al.* (*65*), while tidal mixing was modified for the LGM as in DiNezio *et al.* (*35*).

The standard simulation, experiment LGM_{ref}, uses 21-ka GHG concentrations based on Köhler *et al.* (*66*). It was initialized from the end of a quasi-transient simulation that ran from 24 to 21 ka with an acceleration factor of 5 using GLAC-1D ice sheets. This transient run, in turn, was initialized with a previous CESM LGM simulation (*67*) (initialization method 1). Despite this quasi-transient approach, the deep-ocean trend in the past 100 years of the spin-up is only -0.001 K century^{-1} for temperature and -0.002 psu (practical salinity units) century^{-1} for salinity (global averages at 4000 m).

Three sensitivity experiments serve to explore the role of GHG concentrations: In experiment LGM_{210}, GHG concentrations characteristic for MIS 3 (here 38 ka) from Köhler *et al.* (*66*) were applied. Experiment LGM_{199} uses the average GHG concentrations between LGM_{ref} (21 ka) and LGM_{210} (38 ka). The GHG difference between LGM_{199} and LGM_{ref} was taken and subtracted from LGM_{ref} to obtain an artificially cold climate state in experiment LGM_{176}.

Experiment LGM_{IC} examines the potential role of initial conditions. While the same GHG are used as in experiment LGM_{ref}, the model was initialized from another previous LGM run that used a slightly different model setup with different boundary conditions (*35*) (initialization method 2). Experiment $LGM_{IC,GHG}$ uses still another initialization and GHG concentrations that are slightly different but still characteristic for the LGM. This experiment was initialized from a continuation of another previous CESM LGM simulation (*67*) (initialization method 3).

Experiment LGM_{ICE6G} differs from experiment LGM_{ref} only in the applied ice sheet reconstruction. We used the same land-sea mask as in LGM_{ref} such that the effect of ice sheet height is isolated. The experiment was initialized from the same state as experiment LGM_{ref} (initialization method 1). Additional GHG sensitivity experiments $LGM_{ICE6G,210}$, $LGM_{ICE6G,199}$, and $LGM_{ICE6G,176}$ use different GHG concentrations (see above). All experiments have different integration lengths (as spin-up times turned out to be different) and are summarized in Table 1.

Two-box model

A simple formulation of the salt oscillator consists of two coupled nonlinear autonomous ODEs. The first one describes the change of upper-ocean salinity S_1 in a high-latitude (subpolar) North Atlantic

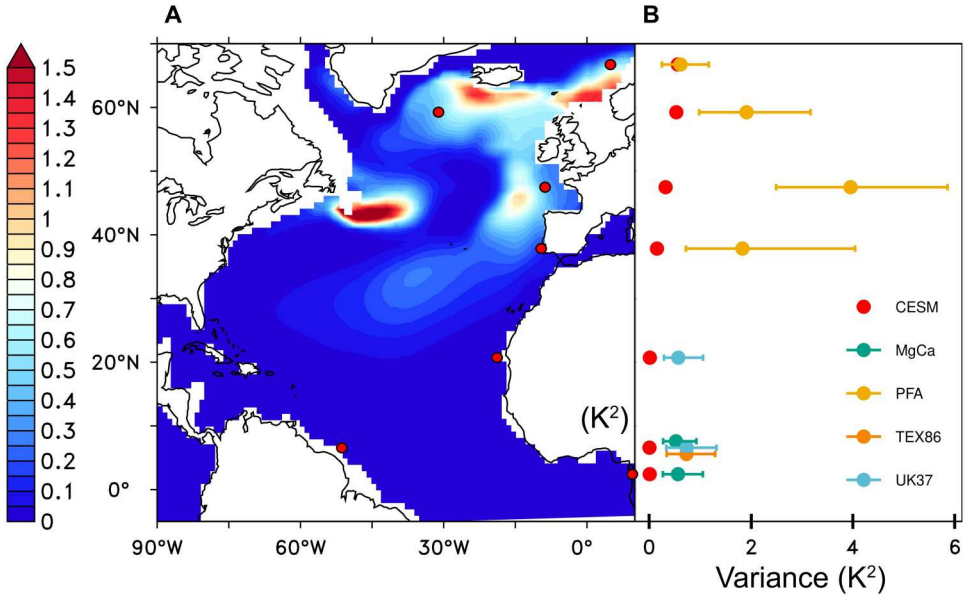

Fig. 9. Model-proxy comparison of multicentennial SST variability during the LGM. (**A**) Variance of modeled summer SST in experiment LGM_{ref} calculated over the entire period of 1540 years after removal of high-frequency variability by means of a 150-year running average. (**B**) Local variances estimated from SST records of North Atlantic sediment cores for the LGM interval 23 to 19 ka at different latitudes. SST time series were first binned at 150 years and high pass–filtered to remove millennial-scale variability. Selection of the records followed strict criteria for age control and resolution. Colors refer to different methods of SST reconstruction. PFA, planktonic foraminifera assemblages. Red dots in (B) show the modeled variances at the core locations marked by the dots in (A). See Materials and Methods for a detailed description of the sediment cores, selection criteria, processing of the time series, and uncertainty estimation. Note that depending on the reconstruction method some records are interpreted as annual mean SST rather than summer SST; however, the large-scale pattern of modeled SST variance is similar for summer and annual mean.

box, while the second one describes the change of upper-ocean salinity S_2 in a low-latitude (subtropical) North Atlantic box (fig. S6). In both boxes, salinity can change because of surface fluxes (net precipitation P over the subpolar box and net evaporation E over the subtropical box) and advective transports by the AMOC with a volume flux q. The AMOC transports low-saline AAIW with a constant salinity S_3 into the subtropical box, from which subtropical water with salinity S_2 is transported into the subpolar box. From here, subpolar water with salinity S_1 is transported into the deep North Atlantic by the downward (convective) limb of the AMOC. This deep-water formation is controlled by the subpolar surface salinity. In the box model, a simple linear relation between AMOC volume flux q and subpolar salinity S_1 is assumed. The system of ODEs thus reads

$$dS_1/dt = (q/V_1) \cdot (S_2 - S_1) - (S_0 \cdot P/D_1) \quad (1)$$

$$dS_2/dt = (q/V_2) \cdot (S_3 - S_2) + (S_0 \cdot E/D_2) \quad (2)$$

with

$$q = k_1 \cdot (S_1 - S_0) + k_2 \quad (3)$$

where S_0 is a constant reference salinity; k_1 and k_2 tune the AMOC volume flux q; V_1 and V_2 are the volumes of the subpolar and subtropical upper-ocean boxes, respectively; D_1 and D_2 are the depths of the subpolar and subtropical upper-ocean boxes; and t is time.

For a particular range of parameters, the system is oscillatory with multicentennial period. Figure S7A shows one possible oscillatory solution using the following set of parameters, which are based on integrated values from the LGM_{ref} simulation: S_0 = 35.5 psu, k_1 = 11.15 Sv psu^{-1}, k_2 = 10 Sv, $V_1 = 25{\cdot}10^6$ km^3, $V_2 = 15{\cdot}10^6$ km^3, D_1 = 2.0 km, D_2 = 1.0 km, P = 0.8 m year^{-1}, E = 1.0 m year^{-1}, and S_3 = 34.4 psu. The ODEs were numerically solved by a simple forward Euler method using a time step of 1 week. Reducing the time step below 1 week has a negligible effect on the solution.

The input of sufficiently fresh AAIW into the subtropical box is crucial for the self-sustained oscillation to occur. The oscillation disappears if the AAIW is too salty, as shown in fig. S7B, where S_3 has been set to 34.7 psu.

Selection and analysis of North Atlantic SST records

SST record selection followed strict criteria for age control and resolution. We only selected time series from the North Atlantic Ocean south of 70°N that covered at least 4000 years within 6 to 0 ka (for the late Holocene analysis of SST variability) or 24 to 18 ka (for the LGM analysis of SST variability) at an average resolution of at least 200 years without a single time step exceeding 1000 years. Minimum requirements for age control were at least two radiocarbon ages with a minimum spacing of 2000 years in the selection interval. Before selection, the age-depth models were recalculated to ensure uniform methodology, estimation of the chronological uncertainty, and calibration to the most recent radiocarbon calibration curve (*68*). The methodology is described in detail elsewhere (*69*). Temperature reconstructions were used as provided by the authors. We averaged reconstructions in cases where multiple reconstructions based on the same sensor were available (e.g., seasonal temperature estimate based on planktonic foraminifera assemblages). The search yielded a total of 11 time series based on different proxies from nine different sites for the Holocene and nine time series from seven sites for the LGM (tables S1 and S2). Only two

time series met the selection criteria for both periods. The time series have an average resolution of 93 and 138 years for the Holocene and LGM period, respectively.

To estimate the SST variances in the late Holocene and LGM intervals, the time series were first binned at 150 years to reduce chronological uncertainty. Subsequently, millennial-scale variability was removed using a high-pass Butterworth filter. The uncertainty of the variance estimates was assessed using a Monte Carlo approach by repeating the calculation over 1000 realizations that accounted for chronological and reconstruction uncertainty of each time series. For simplicity, we assumed a uniform reconstruction uncertainty of 1°C, which is a reasonable approximation (*70*, *71*). We note that the latitudinal pattern in variance is insensitive to a doubling of the uncertainty.

Supplementary Materials

This PDF file includes:

Figs. S1 to S16
Tables S1 and S2
References

REFERENCES AND NOTES

1. T. Laepple, P. Huybers, Ocean surface temperature variability: Large model–data differences at decadal and longer periods. *Proc. Natl. Acad. Sci. U.S.A.* **111**, 16682–16687 (2014).
2. F. Zhu, J. Emile-Geay, N. P. McKay, G. J. Hakim, D. Khider, T. R. Ault, E. J. Steig, S. Dee, J. W. Kirchner, Climate models can correctly simulate the continuum of global-average temperature variability. *Proc. Natl. Acad. Sci. U.S.A.* **116**, 8728–8733 (2019).
3. K. Rehfeld, R. Hébert, J. M. Lora, M. Lofverstrom, C. M. Brierley, Variability of surface climate in simulations of past and future. *Earth Syst. Dynam.* **11**, 447–468 (2020).
4. K. Rehfeld, T. Münch, S. L. Ho, T. Laepple, Global patterns of declining temperature variability from the Last Glacial Maximum to the Holocene. *Nature* **554**, 356–359 (2018).
5. S. van Kreveld, M. Sarnthein, H. Erlenkeuser, P. Grootes, S. Jung, M. Nadeau, U. Pflaumann, A. Voelker, Potential links between surging ice sheets, circulation changes, and the Dansgaard-Oeschger cycles in the Irminger Sea, 60–18 kyr. *Paleoceanogr. Paleoclimatol.* **15**, 425–442 (2000).
6. EPICA Community Members, One-to-one coupling of glacial climate variability in Greenland and Antarctica. *Nature* **444**, 195–198 (2006).
7. P. Kindler, M. Guillevic, M. Baumgartner, J. Schwander, A. Landais, M. Leuenberger, Temperature reconstruction from 10 to 120 kyr b2k from the NGRIP ice core. *Clim. Past* **10**, 887–902 (2014).
8. M. Weinelt, E. Vogelsang, M. Kucera, U. Pflaumann, M. Sarnthein, A. Voelker, H. Erlenkeuser, B. A. Malmgren, Variability of North Atlantic heat transfer during MIS 2. *Paleoceanogr. Paleoclimatol.* **18**, 1071 (2003).
9. M. Schulz, W. H. Berger, M. Sarnthein, P. M. Grootes, Amplitude variations of 1470-year climate oscillations during the last 100,000 years linked to fluctuations of continental ice mass. *Geophys. Res. Lett.* **26**, 3385–3388 (1999).
10. P. Valdes, Built for stability. *Nat. Geosci.* **4**, 414–416 (2011).
11. W. R. Peltier, D. Argus, R. Drummond, Space geodesy constrains ICE age terminal deglaciation: The global ICE-6G_C (VM5a) model. *J. Geophys. Res. Solid Earth* **120**, 450–487 (2015).
12. L. Tarasov, A. S. Dyke, R. M. Neal, W. R. Peltier, A data-calibrated distribution of deglacial chronologies for the North American ice complex from glaciological modeling. *Earth Planet. Sci. Lett.* **315–316**, 30–40 (2012).
13. R. D. Briggs, D. Pollard, L. Tarasov, A data-constrained large ensemble analysis of Antarctic evolution since the Eemian. *Quat. Sci. Rev.* **103**, 91–115 (2014).
14. M. Kageyama, S. Albani, P. Braconnot, S. P. Harrison, P. O. Hopcroft, R. F. Ivanovic, F. Lambert, O. Marti, W. R. Peltier, J.-Y. Peterschmitt, D. M. Roche, L. Tarasov, X. Zhang, E. C. Brady, A. M. Haywood, A. N. LeGrande, D. J. Lunt, N. M. Mahowald, U. Mikolajewicz, K. H. Nisancioglu, B. L. Otto-Bliesner, H. Renssen, R. A. Tomas, Q. Zhang, A. Abe-Ouchi, P. J. Bartlein, J. Cao, Q. Li, G. Lohmann, R. Ohgaito, X. Shi, E. Volodin, K. Yoshida, X. Zhang, W. Zheng, The PMIP4 contribution to CMIP6–Part 4: Scientific objectives and experimental design of the PMIP4-CMIP6 Last Glacial Maximum experiments and PMIP4 sensitivity experiments. *Geosci. Model Dev.* **10**, 4035–4055 (2017).
15. B. R. Crow, M. Prange, M. Schulz, Dynamic boreal summer atmospheric circulation response as negative feedback to Greenland melt during the MIS-11 interglacial. *Clim. Past* **18**, 775–792 (2022).
16. G. Gebbie, How much did glacial North Atlantic water shoal? *Paleoceanogr. Paleoclimatol.* **29**, 190–209 (2014).
17. T. Kurahashi-Nakamura, A. Paul, M. Losch, Dynamical reconstruction of the global ocean state during the Last Glacial Maximum. *Paleoceanogr. Paleoclimatol.* **32**, 326–350 (2017).
18. J. F. Adkins, K. McIntyre, D. P. Schrag, The salinity, temperature, and $\delta^{18}O$ of the glacial deep ocean. *Science* **298**, 1769–1773 (2002).
19. T. L. Insua, A. J. Spivack, D. Graham, S. D'Hondt, K. Moran, Reconstruction of Pacific Ocean bottom water salinity during the Last Glacial Maximum. *Geophys. Res. Lett.* **41**, 2914–2920 (2014).
20. T. A. Ronge, S. Steph, R. Tiedemann, M. Prange, U. Merkel, D. Nürnberg, G. Kuhn, Pushing the boundaries: Glacial/interglacial variability of intermediate and deep waters in the Southwest Pacific over the last 350,000 years. *Paleoceanogr. Paleoclimatol.* **30**, 23–38 (2015).
21. G. Knorr, S. Barker, X. Zhang, G. Lohmann, X. Gong, P. Gierz, C. Stepanek, L. B. Stap, A salty deep ocean as a prerequisite for glacial termination. *Nat. Geosci.* **14**, 930–936 (2021).
22. R. Döscher, C. W. Böning, P. Herrmann, Response of circulation and heat transport in the North Atlantic to changes in thermohaline forcing in northern latitudes: A model study. *J. Phys. Oceanogr.* **24**, 2306–2320 (1994).
23. M. Kawase, Establishment of deep ocean circulation driven by deep-water production. *J. Phys. Oceanogr.* **17**, 2294–2317 (1987).
24. P. Chang, R. Zhang, W. Hazeleger, C. Wen, X. Wan, L. Ji, R. J. Haarsma, W.-P. Breugem, H. Seidel, Oceanic link between abrupt changes in the North Atlantic Ocean and the African monsoon. *Nat. Geosci.* **1**, 444–448 (2008).
25. L. Stramma, F. Schott, The mean flow field of the tropical Atlantic Ocean. *Deep-Sea Res. II Top. Stud. Oceanogr.* **46**, 279–303 (1999).
26. M. Winton, Energetics of deep-decoupling oscillations. *J. Phys. Oceanogr.* **25**, 420–427 (1995).
27. C. Li, A. Born, Coupled atmosphere-ice-ocean dynamics in Dansgaard-Oeschger events. *Quat. Sci. Rev.* **203**, 1–20 (2019).
28. Y. Kuniyoshi, A. Abe-Ouchi, S. Sherriff-Tadano, W.-L. Chan, F. Saito, Effect of climatic precession on Dansgaard-Oeschger-like oscillations. *Geophys. Res. Lett.* **49**, e2021GL095695 (2022).
29. I. M. Held, B. J. Soden, Robust responses of the hydrological cycle to global warming. *J. Clim.* **19**, 5686–5699 (2006).
30. D. Ullman, A. LeGrande, A. E. Carlson, F. Anslow, J. Licciardi, Assessing the impact of Laurentide ice sheet topography on glacial climate. *Clim. Past* **10**, 487–507 (2014).
31. H. J. Andres, L. Tarasov, Towards understanding potential atmospheric contributions to abrupt climate changes: Characterizing changes to the North Atlantic eddy-driven jet over the last deglaciation. *Clim. Past* **15**, 1621–1646 (2019).
32. I. Eisenman, C. M. Bitz, E. Tziperman, Rain driven by receding ice sheets as a cause of past climate change. *Paleoceanogr. Paleoclimatol.* **24**, PA4209 (2009).
33. S. Sherriff-Tadano, A. Abe-Ouchi, A. Oka, Impact of mid-glacial ice sheets on deep ocean circulation and global climate. *Clim. Past* **17**, 95–110 (2021).
34. F. A. Ziemen, C. B. Rodehacke, U. Mikolajewicz, Coupled ice sheet–climate modeling under glacial and preindustrial boundary conditions. *Clim. Past* **10**, 1817–1836 (2014).
35. P. N. DiNezio, J. E. Tierney, B. L. Otto-Bliesner, A. Timmermann, T. Bhattacharya, N. Rosenbloom, E. Brady, Glacial changes in tropical climate amplified by the Indian Ocean. *Sci. Adv.* **4**, eaat9658 (2018).
36. M. Kageyama, S. P. Harrison, M.-L. Kapsch, M. Lofverstrom, J. M. Lora, U. Mikolajewicz, S. Sherriff-Tadano, T. Vadsaria, A. Abe-Ouchi, N. Bouttes, D. Chandan, L. J. Gregoire, R. F. Ivanovic, K. Izumi, A. N. LeGrande, F. Lhardy, G. Lohmann, P. A. Morozova, R. Ohgaito, A. Paul, W. R. Peltier, C. J. Poulsen, A. Quiquet, D. M. Roche, X. Shi, J. E. Tierney, P. J. Valdes, E. Volodin, J. Zhu, The PMIP4 Last Glacial Maximum experiments: Preliminary results and comparison with the PMIP3 simulations. *Clim. Past* **17**, 1065–1089 (2021).
37. T. Laepple, P. Huybers, Reconciling discrepancies between Uk37 and mg/ca reconstructions of Holocene marine temperature variability. *Earth Planet. Sci. Lett.* **375**, 418–429 (2013).
38. X. Zhang, M. Prange, U. Merkel, M. Schulz, Spatial fingerprint and magnitude of changes in the Atlantic meridional overturning circulation during marine isotope stage 3. *Geophys. Res. Lett.* **42**, 1903–1911 (2015).
39. A. Ganopolski, S. Rahmstorf, Rapid changes of glacial climate simulated in a coupled climate model. *Nature* **409**, 153–158 (2001).
40. L. Menviel, A. Timmermann, T. Friedrich, M. England, Hindcasting the continuum of Dansgaard–Oeschger variability: Mechanisms, patterns and timing. *Clim. Past* **10**, 63–77 (2014).

41. W. R. Peltier, G. Vettoretti, Dansgaard-Oeschger oscillations predicted in a comprehensive model of glacial climate: A "kicked" salt oscillator in the Atlantic. *Geophys. Res. Lett.* **41**, 7306–7313 (2014).
42. F. Eynaud, B. Malaizé, S. Zaragosi, A. de Vernal, J. Scourse, C. Pujol, E. Cortijo, F. E. Grousset, A. Penaud, S. Toucanne, J.-L. Turon, G. Auffret, New constraints on European glacial freshwater releases to the North Atlantic Ocean. *Geophys. Res. Lett.* **39**, L15601 (2012).
43. A. H. Voelker, Global distribution of centennial-scale records for marine isotope stage (MIS) 3: A database. *Quat. Sci. Rev.* **21**, 1185–1212 (2002).
44. G. Vettoretti, W. R. Peltier, Fast physics and slow physics in the nonlinear Dansgaard–Oeschger relaxation oscillation. *J. Clim.* **31**, 3423–3449 (2018).
45. N. Brown, E. D. Galbraith, Hosed vs. unhosed: Interruptions of the Atlantic meridional overturning circulation in a global coupled model, with and without freshwater forcing. *Clim. Past* **12**, 1663–1679 (2016).
46. E. Armstrong, K. Izumi, P. Valdes, Identifying the mechanisms of DO-scale oscillations in a GCM: A salt oscillator triggered by the Laurentide ice sheet. *Climate Dynam.* **60**, 3983–4001 (2023).
47. W. R. Peltier, Y. Ma, D. Chandan, The KPP trigger of rapid AMOC intensification in the nonlinear Dansgaard-Oeschger relaxation oscillation. *J. Geophys. Res. Oceans* **125**, e2019JC015557 (2020).
48. G. Vettoretti, P. Ditlevsen, M. Jochum, S. O. Rasmussen, Atmospheric CO_2 control of spontaneous millennial-scale ice age climate oscillations. *Nat. Geosci.* **15**, 300–306 (2022).
49. Y. Romé, R. F. Ivanovic, L. J. Gregoire, S. Sherriff-Tadano, P. J. Valdes, Millennial-scale climate oscillations triggered by deglacial meltwater discharge in Last Glacial Maximum simulations. *Paleoceanogr. Paleoclimatol.* **37**, e2022PA004451 (2022).
50. I. Malmierca-Vallet, L. C. Sime; D-O community members, Dansgaard–Oeschger events in climate models: Review and baseline marine isotope stage 3 (MIS3) protocol. *Clim. Past* **19**, 915–942 (2023).
51. G. Vettoretti, W. R. Peltier, Thermohaline instability and the formation of glacial North Atlantic super polynyas at the onset of Dansgaard-Oeschger warming events. *Geophys. Res. Lett.* **43**, 5336–5344 (2016).
52. D. W. Pierce, T. P. Barnett, U. Mikolajewicz, Competing roles of heat and freshwater flux in forcing thermohaline oscillations. *J. Phys. Oceanogr.* **25**, 2046–2064 (1995).
53. S. Drijfhout, C. Heinze, M. Latif, E. Maier-Reimer, Mean circulation and internal variability in an ocean primitive equation model. *J. Phys. Oceanogr.* **26**, 559–580 (1996).
54. T. J. Osborn, Thermohaline oscillations in the LSG OGCM: Propagating anomalies and sensitivity to parameterizations. *J. Phys. Oceanogr.* **27**, 2233–2255 (1997).
55. W. Park, M. Latif, Multidecadal and multicentennial variability of the meridional overturning circulation. *Geophys. Res. Lett.* **35**, L22703 (2008).
56. T. Martin, W. Park, M. Latif, Multi-centennial variability controlled by Southern Ocean convection in the Kiel climate model. *Clim. Dyn.* **40**, 2005–2022 (2013).
57. U. Mikolajewicz, E. Maier-Reimer, Internal secular variability in an ocean general circulation model. *Clim. Dyn.* **4**, 145–156 (1990).
58. M. Winton, E. S. Sarachik, Thermohaline oscillations induced by strong steady salinity forcing of ocean general circulation models. *J. Phys. Oceanogr.* **23**, 1389–1410 (1993).
59. F. Sévellec, T. Huck, M. Ben Jelloul, On the mechanism of centennial thermohaline oscillations. *J. Mar. Res.* **64**, 355–392 (2006).
60. T. L. Delworth, F. Zeng, Multicentennial variability of the Atlantic meridional overturning circulation and its climatic influence in a 4000 year simulation of the GFDL CM2.1 climate model. *Geophys. Res. Lett.* **39**, L13702 (2012).
61. W. Jiang, G. Gastineau, F. Codron, Multicentennial variability driven by salinity exchanges between the Atlantic and the Arctic Ocean in a coupled climate model. *J. Adv. Model. Earth Syst.* **13**, e2020MS002366 (2021).
62. V. L. Meccia, R. Fuentes-Franco, P. Davini, K. Bellomo, F. Fabiano, S. Yang, J. von Hardenberg, Internal multi-centennial variability of the Atlantic meridional overturning circulation simulated by EC-Earth3. *Clim. Dyn.* **60**, 3695–3712 (2023).
63. O. Mehling, K. Bellomo, M. Angeloni, C. Pasquero, J. von Hardenberg, High-latitude precipitation as a driver of multicentennial variability of the AMOC in a climate model of intermediate complexity. *Clim. Dyn.* **61**, 1519–1534 (2023).
64. J. W. Hurrell, M. M. Holland, P. R. Gent, S. Ghan, J. E. Kay, P. J. Kushner, J.-F. Lamarque, W. G. Large, D. Lawrence, K. Lindsay, W. H. Lipscomb, M. C. Long, N. Mahowald, D. R. Marsh, R. B. Neale, P. Rasch, S. Vavrus, M. Vertenstein, D. Bader, W. D. Collins, J. J. Hack, J. Kiehl, S. Marshall, The Community Earth System Model: A framework for collaborative research. *Bull. Am. Meteorol. Soc.* **94**, 1339–1360 (2013).
65. E. C. Brady, B. L. Otto-Bliesner, J. E. Kay, N. Rosenbloom, Sensitivity to glacial forcing in the CCSM4. *J. Clim.* **26**, 1901–1925 (2013).
66. P. Köhler, C. Nehrbass-Ahles, J. Schmitt, T. F. Stocker, H. Fischer, A 156 kyr smoothed history of the atmospheric greenhouse gases CO_2, CH_4 and N_2O and their radiative forcing. *Earth Syst. Sci. Data* **9**, 363–387 (2017).
67. P. Bakker, I. Rogozhina, U. Merkel, M. Prange, Hypersensitivity of glacial summer temperatures in Siberia. *Clim. Past* **16**, 371–386 (2020).
68. P. J. Reimer, W. E. Austin, E. Bard, A. Bayliss, P. G. Blackwell, C. B. Ramsey, M. Butzin, H. Cheng, R. L. Edwards, M. Friedrich, P. M. Grootes, T. P. Guilderson, I. Hajdas, T. J. Heaton, A. G. Hogg, K. A. Hughen, B. Kromer, S. W. Manning, R. Muscheler, J. G. Palmer, C. Pearson, J. van der Plicht, R. W. Reimer, D. A. Richards, E. M. Scott, J. R. Southon, C. S. M. Turney, L. Wacker, F. Adolphi, U. Büntgen, M. Capano, S. M. Fahrni, A. Fogtmann-Schulz, R. Friedrich, P. Köhler, S. Kudsk, F. Miyake, J. Olsen, F. Reinig, M. Sakamoto, A. Sookdeo, S. Talamo, The IntCal20 Northern Hemisphere radiocarbon age calibration curve (0–55 cal kBP). *Radiocarbon* **62**, 725–757 (2020).
69. L. Jonkers, O. Cartapanis, M. Langner, N. McKay, S. Mulitza, A. Strack, M. Kucera, Integrating palaeoclimate time series with rich metadata for uncertainty modelling: Strategy and documentation of the PalMod 130k marine palaeoclimate data synthesis. *Earth Syst. Sci. Data* **12**, 1053–1081 (2020).
70. M. Kucera, M. Weinelt, T. Kiefer, U. Pflaumann, A. Hayes, M. Weinelt, M.-T. Chen, A. C. Mix, T. T. Barrows, E. Cortijo, J. Duprat, S. Juggins, C. Waelbroeck, Reconstruction of sea-surface temperatures from assemblages of planktonic foraminifera: Multi-technique approach based on geographically constrained calibration data sets and its application to glacial Atlantic and Pacific Oceans. *Quat. Sci. Rev.* **24**, 951–998 (2005).
71. J. E. Tierney, M. P. Tingley, BAYSPLINE: A new calibration for the alkenone paleothermometer. *Paleoceanogr. Paleoclimatol.* **33**, 281–301 (2018).
72. C. Torrence, G. P. Compo, A practical guide to wavelet analysis. *Bull. Am. Meteorol. Soc.* **79**, 61–78 (1998).
73. E. Vogelsang, U. Pflaumann, M. Sarnthein, "$\delta^{18}O$ stratigraphy, chronology, and sea surface temperatures of Atlantic sediment records (GLAMAP-2000 Kiel)" (Report, Inst. f. Geowissenschaften, Christian-Albrechts-Universität, 2001).
74. A. H. Voelker, L. de Abreu, A review of abrupt climate change events in the Northeastern Atlantic Ocean (Iberian Margin): Latitudinal, longitudinal, and vertical gradients, in *Abrupt Climate Change: Mechanisms, Patterns, and Impacts* (2011), Geophysical Monograph Series, AGU, Washington DC, vol. 193, pp. 15–37.
75. M. Zhao, N. Beveridge, N. Shackleton, M. Sarnthein, G. Eglinton, Molecular stratigraphy of cores off Northwest Africa: Sea surface temperature history over the last 80 ka. *Paleoceanogr. Paleoclimatol.* **10**, 661–675 (1995).
76. S. Crivellari, C. M. Chiessi, H. Kuhnert, C. Häggi, G. Mollenhauer, J. Hefter, R. Portilho-Ramos, E. Schefuß, S. Mulitza, Thermal response of the western tropical Atlantic to slowdown of the Atlantic meridional overturning circulation. *Earth Planet. Sci. Lett.* **519**, 120–129 (2019).
77. A. Jennings, J. Andrews, C. Pearce, L. Wilson, S. Ólfasdóttir, Detrital carbonate peaks on the Labrador shelf, a 13–7 ka template for freshwater forcing from the Hudson Strait outlet of the Laurentide ice sheet into the subpolar gyre. *Quat. Sci. Rev.* **107**, 62–80 (2015).
78. B. Risebrobakken, T. Dokken, L. H. Smedsrud, C. Andersson, E. Jansen, M. Moros, E. V. Ivanova, Early Holocene temperature variability in the Nordic seas: The role of oceanic heat advection versus changes in orbital forcing. *Paleoceanogr. Paleoclimatol.* **26**, PA4206 (2011).
79. D. J. Thornalley, H. Elderfield, I. N. McCave, Holocene oscillations in temperature and salinity of the surface subpolar North Atlantic. *Nature* **457**, 711–714 (2009).
80. R. E. Came, D. W. Oppo, J. F. McManus, Amplitude and timing of temperature and salinity variability in the subpolar North Atlantic over the past 10 ky. *Geology* **35**, 315–318 (2007).
81. O. Marchal, I. Cacho, T. F. Stocker, J. O. Grimalt, E. Calvo, B. Martrat, N. Shackleton, M. Vautravers, E. Cortijo, S. van Kreveld, Apparent long-term cooling of the sea surface in the Northeast Atlantic and Mediterranean during the Holocene. *Quat. Sci. Rev.* **21**, 455–483 (2002).
82. T. Rodrigues, J. O. Grimalt, F. Abrantes, F. Naughton, J.-A. Flores, The last glacial–interglacial transition (LGIT) in the western mid-latitudes of the North Atlantic: Abrupt sea surface temperature change and sea level implications. *Quat. Sci. Rev.* **29**, 1853–1862 (2010).
83. J. Schirrmacher, M. Weinelt, T. Blanz, N. Andersen, E. Salgueiro, R. R. Schneider, Multidecadal atmospheric and marine climate variability in southern Iberia during the mid- to late-Holocene. *Clim. Past* **15**, 617–634 (2019).
84. J.-H. Kim, N. Rimbu, S. J. Lorenz, G. Lohmann, S.-I. Nam, S. Schouten, C. Rühlemann, R. R. Schneider, North Pacific and North Atlantic sea-surface temperature variability during the Holocene. *Quat. Sci. Rev.* **23**, 2141–2154 (2004).
85. P. DeMenocal, J. Ortiz, T. Guilderson, M. Sarnthein, Coherent high- and low-latitude climate variability during the Holocene warm period. *Science* **288**, 2198–2202 (2000).
86. S. Weldeab, D. W. Lea, R. R. Schneider, N. Andersen, 155,000 years of West African monsoon and ocean thermal evolution. *Science* **316**, 1303–1307 (2007).

Acknowledgments: We gratefully acknowledge the computing time granted by the Resource Allocation Board and provided on the supercomputer Lise and Emmy at NHR@ZIB and NHR@Göttingen as part of the NHR infrastructure. We would like to thank S. Mulitza, M. Kucera, and G. Knorr for stimulating discussions. **Funding:** This research was funded by the German

Federal Ministry of Education and Science (BMBF) through the "PalMod" project under grant numbers 01LP1915B, 01LP1916C, and 01LP1922A and by the Cluster of Excellence EXC 2077 ("The Ocean Floor—Earth's Uncharted Interface"). **Author contributions:** Conceptualization: M.P. designed the study. Methodology: M.P., U.M., and P.B. set up and carried out CESM simulations. L.J. compiled proxy records. Investigation: M.P. analyzed CESM model output and NGRIP data and formulated box model. L.J. analyzed marine proxy records. All coauthors discussed results. Visualization: M.P. and L.J. produced the figures. Writing: M.P. wrote the manuscript with input from all coauthors. **Competing interests:** The authors declare that they have no competing interests. **Data and materials availability:** All data needed to evaluate the conclusions in the paper are present in the paper and/or the Supplementary Materials. Climate model output data are available at https://zenodo.org/record/8341426. Proxy record availability as indicated in tables S1 and S2. Box-model code is available at https://zenodo.org/record/8341368.

Submitted 10 February 2023
Accepted 29 September 2023
Published 1 November 2023
10.1126/sciadv.adh1106

Science Advances

A multicentennial mode of North Atlantic climate variability throughout the Last Glacial Maximum

Matthias Prange, Lukas Jonkers, Ute Merkel, Michael Schulz, and Pepijn Bakker

Sci. Adv. **9** (44), eadh1106. DOI: 10.1126/sciadv.adh1106

Science Advances (ISSN 2375-2548) is published by the American Association for the Advancement of Science. 1200 New York Avenue NW, Washington, DC 20005. The title *Science Advances* is a registered trademark of AAAS.